

Accurate metrology of polarization curves measured at the speckle size of visible light scattering

A. Ghabbach, M. Zerrad, G. Soriano, and C. Amra*

Aix Marseille Université, CNRS, Centrale Marseille, Institut Fresnel, UMR 7249, 13013 Marseille, France

*claude.amra@fresnel.fr

Abstract: An optical procedure is presented to measure at the speckle size and with high accuracy, the polarization degree of patterns scattered by disordered media. Whole mappings of polarization ratio, polarimetric phase and polarization degree are pointed out. Scattered clouds are emphasized on the Poincaré sphere, and are completed by probability density functions of the polarization degree. A special care is attributed to the accuracy of data. The set-up provides additional signatures of scattering media.

©2014 Optical Society of America

OCIS codes: (030.6140) Speckle; (260.2130) Ellipsometry and polarimetry; (260.5430) Polarization; (290.5855) Scattering, polarization; (120.3930) Metrological instrumentation; (120.3940) Metrology.

References and links

1. E. Wolf and L. Mandel, *Optical Coherence and Quantum Optics* (Cambridge University, 1995)
2. C. Brosseau, *Fundamentals of Polarized Light - A Statistical Approach* (Wiley, 1998)
3. J. W. Goodman, *Statistical Optics* (Wiley- Interscience, 2000).
4. E. Jakeman and K. D. Ridley, *Modeling Fluctuations in Scattered Waves* (Taylor and Francis Group, 2006)
5. E. Wolf, *Theory of coherence and polarization of light* (Cambridge University, ed. 2007)
6. R. Barakat, "Polarization entropy transfer and relative polarization entropy," *Opt. Commun.* **123**(4-6), 443–448 (1996).
7. P. Réfrégier and A. Luis, "Irreversible effects of random unitary transformations on coherence properties of partially polarized electromagnetic fields," *J. Opt. Soc. Am. A* **25**(11), 2749–2757 (2008).
8. H. D. Noble and R. A. Chipman, "Mueller matrix roots algorithm and computational considerations," *Opt. Express* **20**(1), 17–31 (2012).
9. N. Ortega-Quijano and J. L. Arce-Diego, "Mueller matrix differential decomposition for direction reversal: application to samples measured in reflection and backscattering," *Opt. Express* **19**(15), 14348–14353 (2011).
10. J. W. Goodman, *Speckle Phenomena in Optics: Theory and Applications* (Roberts and Company Publishers, 2007)
11. J. Sorrentini, M. Zerrad, and C. Amra, "Statistical signatures of random media and their correlation to polarization properties," *Opt. Lett.* **34**(16), 2429–2431 (2009).
12. S. G. Hanson and H. T. Yura, "Statistics of spatially integrated speckle intensity difference," *J. Opt. Soc. Am. A* **26**(2), 371–375 (2009).
13. M. Zerrad, J. Sorrentini, G. Soriano, and C. Amra, "Gradual loss of polarization in light scattered from rough surfaces: Electromagnetic prediction," *Opt. Express* **18**(15), 15832–15843 (2010).
14. J. Sorrentini, M. Zerrad, G. Soriano, and C. Amra, "Enpolarization of light by scattering media," *Opt. Express* **19**(22), 21313–21320 (2011).
15. P. Réfrégier, M. Zerrad, and C. Amra, "Coherence and polarization properties in speckle of totally depolarized light scattered by totally depolarizing media," *Opt. Lett.* **37**(11), 2055–2057 (2012).
16. M. Zerrad, G. Soriano, A. Ghabbach, and C. Amra, "Light enpolarization by disordered media under partial polarized illumination: The role of cross-scattering coefficients," *Opt. Express* **21**(3), 2787–2794 (2013).
17. G. Soriano, M. Zerrad, and C. Amra, "Mapping the coherence time of far-field speckle scattered by disordered media," *Opt. Express* **21**(20), 24191–24200 (2013).
18. B. DeBoo, J. Sasian, and R. Chipman, "Degree of polarization surfaces and maps for analysis of depolarization," *Opt. Express* **12**(20), 4941–4958 (2004).
19. O. V. Angelsky, S. G. Hanson, C. Yu. Zenkova, M. P. Gorsky, and N. V. Gorodys'ka, "On polarization metrology (estimation) of the degree of coherence of optical waves," *Opt. Express* **17**(18), 15623–15634 (2009).
20. F. Goudail and A. Bénére, "Estimation precision of the degree of linear polarization and of the angle of polarization in the presence of different sources of noise," *Appl. Opt.* **49**(4), 683–693 (2010).

21. B. H. Ibrahim, S. B. Hatit, and A. De Martino, "Angle resolved Mueller polarimetry with a high numerical aperture and characterization of transparent biaxial samples," *Appl. Opt.* **48**(27), 5025–5034 (2009).
 22. L. Pouget, J. Fade, C. Hamel, and M. Alouini, "Polarimetric imaging beyond the speckle grain scale," *Appl. Opt.* **51**(30), 7345–7356 (2012).
 23. J. Ellis, A. Dogariu, S. Ponomarenko, and E. Wolf, "Correlation matrix of a completely polarized, statistically stationary electromagnetic field," *Opt. Lett.* **29**(13), 1536–1538 (2004).
 24. J. Broky and A. Dogariu, "Complex degree of mutual polarization in randomly scattered fields," *Opt. Express* **18**(19), 20105–20113 (2010).
 25. J. Broky and A. Dogariu, "Correlations of polarization in random electro-magnetic fields," *Opt. Express* **19**(17), 15711–15719 (2011).
-

1. Introduction

Light polarization still remains the focus of numerous works. Theoretical tools [1–5] have now unified polarization and coherence (spatial and temporal), and an increasing number of papers gather polarization and entropy [6,7], Mueller matrix factorization [8,9], electromagnetic and statistical optics [10], and speckle histograms [11]. A special care has recently [12,13] been attributed to local (temporal) and global (spatial) depolarization; repolarization effects [14–16] were also emphasized in disordered media, speckle histograms were used to separate surface and bulk origins [11], and the coherence time of scattering patterns was mapped in the far field [17].

At this stage of investigation, experimental techniques for the polarization metrology play an increasing role, at least to check assumptions of the theoretical models and validate the origins of phenomena. Several techniques have been used for decades to measure light polarization [18–22]. Among them ellipsometry is well known, with different techniques (rotating analyzers, photo-acoustic modulators...) to vary or generate the field polarization, while LCD devices today offer alternative solutions. However most techniques were firstly devoted to specular (direct) optics, and they sometimes fail when light polarization must be analyzed at the speckle size of a scattering pattern emitted by a disordered medium [23–25]. Indeed specific difficulties occur at this scale with a first difficulty connected with the number of speckle grains to analyze in the scattering pattern, in opposition with the unique direction of specular optics (reflection or transmission). Other difficulties are related to the low scattering levels, the temporal stability... Furthermore, due to the fine speckle structure, any mechanical movement (such as rotating polarizers) should be prevented in a measurement procedure.

Polarization measurements hence involve an increased complexity when disordered media are investigated. Classical Stokes techniques involving a few polarization data have been extensively used for specular optics, and sometimes can be generalized to scattering patterns. However great advantages can also be provided when a complete polarization curve is measured at the speckle size, in order to check or identify the physical process under investigation. Such "local" ellipsometric curves confer additional information and accuracy to the polarization data, and help to cancel potential errors or bias resulting from the signal to noise ratio, or from a temporal shift (thermal, mechanical) connected with devices in the optical system (source, sample, polarizers...). Moreover, statistical tools may surely bring more robustness via emphasis on the different moments of all data.

Within this framework we developed a specific set-up to measure a complete polarization curve within each grain of a speckle pattern emitted in the far field by a disordered medium (rough surfaces and inhomogeneous bulks). The local (temporal) degree of polarization is analyzed in detail in the whole scattering pattern and we emphasize its spatial or angular variations on the Poincaré sphere, in connection with the incident polarization, the nature of sample and the energy levels. Additional histograms and probability density functions are measured to point out the performance limits of the system, or to reveal accurate signatures of scattering patterns. And in a more general way, these experimental data validate and complete the theoretical predictions which were given in previous papers [13,16] on the basis on

phenomenological (statistical) and electromagnetic approaches. Applications concern probing of disordered media (living or mineral tissues) and imaging in diffusive media.

2. Principles and procedures

In what follows all media are assumed to be linear and isotropic, and the incident light is collimated, quasi-monochromatic and coherent. We use the analytic (complex) signal representation.

2.1 Polarization curve

At the entrance of the polarization analysis system (Fig. 1), the field is written as $\mathbf{E}(t) = \mathbf{E}_S(t) + \mathbf{E}_P(t)$, with E_S and E_P the orthogonal polarization modes in a plane perpendicular to the propagation direction. This field passes through two optical devices that are first a retardation plate, and then an analyzer. The resulting algebraic amplitude in the analyzer direction is given by:

$$E'(t) = \cos \phi E_S(t) \exp(j\eta_S) + \sin \phi E_P(t) \exp(j\eta_P) \quad (1)$$

with ϕ the angle specific of the analyzer direction with respect to the S-mode, and (η_S, η_P) the phase action of the retarder on the polarization modes.

At the system output light is collected by a low frequency quadratic detector which delivers a constant voltage V proportional to a time average signal of the square optical field, that is:

$$V = K \left\{ \cos^2 \phi \langle |E_S(t)|^2 \rangle + \sin^2 \phi \langle |E_P(t)|^2 \rangle \right\} + 2 \cos \phi \sin \phi \Re \left\{ \langle E_S(t) E_P^*(t) \rangle \exp(j\eta) \right\} \quad (2)$$

with $\langle \rangle$ the time average, K a proportionality factor inherent to calibration, and $\eta = \eta_S - \eta_P$ the polarimetric phase difference given by the retardation plate. Now introducing the polarization ratio $\beta = [\langle E_P^2(t) \rangle / \langle E_S^2(t) \rangle]^{0.5}$, and the mutual coherence $\mu = \langle E_S(t) E_P^*(t) \rangle / [\langle |E_S(t)|^2 \rangle \langle |E_P(t)|^2 \rangle]^{0.5}$, relation (2) is transformed as:

$$V(\phi, \eta) = K \cos^2 \phi \langle |E_S(t)|^2 \rangle \left\{ 1 + \beta^2 \tan^2 \phi + 2\beta |\mu| \tan \phi \cos(\delta + \eta) \right\} \quad (3)$$

with $\delta = \text{Arg}(\mu)$ the phase of mutual coherence. At this step the polarization state is fully characterized by the polarization curve $V(\phi, \eta)$ whose tunable variables are the analyzer angle ϕ and the phase retardation η . Then a complete analysis of this curve would allow to extract the three (β, μ, δ) unknown parameters in order to reach the polarization ellipse together with the local degree of polarization (dop) following:

$$DOP^2 = 1 - 4 \frac{\beta}{(1+\beta)^2} (1 - |\mu|^2) \quad (4)$$

2.2 Extraction of first parameters

Equation (3) can again be written as:

$$V(\phi, \eta) = \gamma(\phi) \{ 1 + \alpha(\phi) \cos(\delta + \eta) \} \quad (5)$$

with:

$$\gamma(\phi) = K \cos^2 \phi \langle |E_S(t)|^2 \rangle \{ 1 + \beta^2 \tan^2 \phi \} \quad (6)$$

and

$$\alpha(\phi) = \frac{2\beta|\mu|\tan\phi}{1 + \beta^2 \tan^2\phi} \quad (7)$$

Due to the fine speckle structure, any mechanical movement is here prohibited, so that the analyzer angle (ϕ) is fixed in a first step. Then we use the LCD voltage (v) to scan the retardation $\eta(v)$ of the LCD device, and the scattering signal (V_k) is recorded for a series of N polarimetric phases η_k , that are:

$$V_k = V(\phi, \eta_k) = \gamma(\phi) \{1 + \alpha(\phi) \cos(\delta + \eta_k)\} \quad (8)$$

Provided that the phase data η_k are adequately distributed within $[0, 2\pi]$, the coefficient γ can first be given by an average over one period with N data points:

$$\langle V_k \rangle_k = \frac{1}{N} \sum_k V_k = \gamma(\phi) \quad (9)$$

which allows to consider a normalized signal in the simplified form:

$$M_k(\phi) = \frac{V_k}{\langle V_k \rangle} = 1 + \alpha(\phi) \cos(\delta + \eta_k) \quad (10)$$

At this step the following curve is directly accessible to experiment:

$$N_k(\phi) = M_k(\phi) - 1 = \alpha(\phi) \cos(\delta + \eta_k) \quad (11)$$

and the measured value is denoted N'_k . Then we use a Least Mean Square (LMS) criteria to minimize the merit function:

$$F(\alpha, \delta) = \frac{1}{N} \sum_k [N'_k - \alpha(\phi) \cos(\delta + \eta_k)]^2 \quad (12)$$

One can easily check that minimization allows to reach the following analytical formulae for the two parameters α and δ :

$$\alpha = \frac{2}{N} \sqrt{\left[\sum_k N'_k(\phi) \cos(\eta_k) \right]^2 + \left[\sum_k N'_k(\phi) \sin(\eta_k) \right]^2} > 0 \quad (13)$$

$$\cos \delta = \frac{2}{N \alpha} \sum_k N'_k(\phi) \cos(\eta_k) \quad (14)$$

$$\sin \delta = \frac{2}{N \alpha} \sum_k N'_k(\phi) \sin(\eta_k) \quad (15)$$

and this procedure must be applied for each pixel ij of the CCD camera.

3. Polarization parameters

At this step the correlation phase δ is known but the α value given in Eq. (7) does not allow to separate the ($\beta, |\mu|$) parameters, what is required to express the polarization degree following Eq. (4). In case where $\beta = 1$, we know that $\text{dop} = |\mu|$, but the procedure should be completed to investigate the general case of partial polarization. For that a second LMS procedure can be used with an additional scan over the analyzer angle ϕ , hence providing the $\alpha(\phi)$ function. To

avoid any mechanical movement, a tunable (voltage) polarization rotator is used rather than a rotating analyzer. Equation (3) still remains valid provided that ϕ is now the rotator angle.

Consider now that the $\alpha(\phi)$ function of Eq. (13) is measured over the η_k values for each ϕ value, and let us denote by α'_q the measured values over Q data. One can check again that the LMS procedure over the ϕ_q values first leads to:

$$|\mu| = \frac{\sum_q \alpha'_q u_q}{\sum_q u_q^2} = f(\beta) \quad (16)$$

$$\text{with } u_q = \frac{2\beta \tan \phi_q}{1 + \beta^2 \tan^2 \phi_q}$$

This first relation gives $|\mu|$ versus the polarization ratio β , so that the second LMS relation is required. It is given by:

$$|\mu| = \frac{\sum_q \alpha'_q \tan \phi_q \frac{1 - \beta^2 \tan^2 \phi_q}{(1 + \beta^2 \tan^2 \phi_q)^2}}{2\beta \sum_q \alpha'_q \tan^2 \phi_q \frac{1 - \beta^2 \tan^2 \phi_q}{(1 + \beta^2 \tan^2 \phi_q)^3}} = g(\beta) \quad (17)$$

At this step Eqs. (16)-(17) allow to determine both β and μ in a numerical way at the intersection of the $f(\beta)$ and $g(\beta)$ functions, which allows the dop determination.

However this second LMS procedure (additional scan over the ϕ values) would increase the acquisition time from some minutes to a few hours, which is prohibitive. To solve this point we proceeded in a different way with only two ϕ values. The first value $\phi = 0^\circ$ allows to write:

$$V(\phi = 0) = V_0 = \gamma_0 = K \langle |E_s(t)|^2 \rangle \quad (18-a)$$

and the accuracy can be improved with an average over η :

$$\langle V_0 \rangle_\eta = \gamma_0 = K \langle |E_s(t)|^2 \rangle \quad (18-b)$$

The second value $\phi = \pi/4$ requires to take an average over η , that is:

$$\langle V(\phi = 45^\circ) \rangle_\eta = \langle V_{45} \rangle_\eta = \gamma_{45} (1 + \beta^2) = \frac{1}{2} K \langle |E_s(t)|^2 \rangle (1 + \beta^2) \quad (19)$$

Equations (16)-(17) now give the polarization ratio β and allow to write the modulus $|\mu|$ of the complex correlation versus β as follows:

$$\beta = \sqrt{-1 + 2 \frac{\langle V_{45} \rangle}{\langle V_0 \rangle}} \quad (20-a)$$

$$|\mu| = \alpha_{45} \frac{1 + \beta^2}{2\beta} \quad (20-b)$$

Since α_{45} is already known from the first LMS procedure at $\phi = \pi/4$, all parameters can now be extracted for each pixel of the CCD camera.

4. Validation with specular optics

A first step now consists in the validation of the previous procedure, whose performances must be analyzed in detail. Indeed scattering patterns in the next section may raise a number of unexpected phenomena whose origins should not be confused with an uncertainty of measurements or a bias in the methods. For this reason we are here concerned by a calibration or a reference in the measurement system, and this reference will be provided by the analysis of the incident beam polarization; such investigation will allow us in a second step to study the properties of the scattering patterns in regard to those of the incident beam.

For that we used the set-up of Fig. 1 where an un-polarized laser beam (633nm He-Ne laser, 10mW power) passes through a polarizer at 45°, hence providing a 45° full linear polarization at the system entrance. The receiver at the output system is a CCD camera with 1024x1024 pixels of 13μm size.

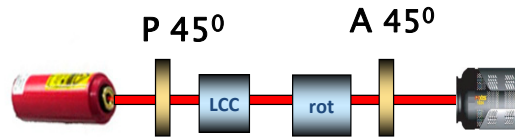


Fig. 1. Basic polarization set-up for specular optics.

Each camera pixel (ij) would now deliver a voltage signal V_{ij} in a form which follows Eq. (5), that is:

$$V_{ij}(\phi, \eta_k) = V_{ij}(\phi) = \gamma_{ij}(\phi) \left[1 + \alpha_{ij}(\phi) \cos(\delta_{ij} + \eta_k) \right] \quad (21)$$

with

$$\alpha_{ij}(\phi) = 2\beta_{ij} \left| \mu_{ij} \right| \frac{\tan \phi}{1 + \beta_{ij}^2 \tan^2 \phi} \quad (22)$$

and

$$\gamma_{ij}(\phi) = K \cos^2 \phi \left\langle \left| E_{S,ij}(t) \right|^2 \right\rangle \left\{ 1 + \beta_{ij}^2 \tan^2 \phi \right\} \quad (23)$$

Each V_{ijk} measurement would require a specific integration time Δt_{ijk} , but the camera does not offer this opportunity (all pixels must have the same Δt). Hence the integration time is tuned at each phase value η_k for all pixels, that is: $\Delta t_{ijk} = \Delta t_k$. Such limitation does not prevent from reaching high quality data, in particular for the direct beam. Indeed the single geometry (specular) of the direct beam makes all pixel signals V_{ij} to vary in a similar form given by:

$$V_{ij}(\phi = 45^\circ) \approx K \left\langle \left| E_{S,ij} \right|^2 \right\rangle \left[1 + \cos(\eta_k) \right] \quad (24)$$

This is classical and due to the fact that the polarization properties of the entrance beam are expected to be uniform within the camera area, with a zero correlation phase ($\delta_{ij} = \delta \approx 0$) and a unity polarization ratio ($\beta_{ij} = \beta \approx 1$). Therefore all pixel curves $V_{ij}(\eta_k)$ are roughly proportional so that the integration time can be adjusted for each η_k value to satisfy an accurate measurement of the maximum grey level, that is $\max_{ij}(V_{ijk})$ over the ij data. In this case the maximum is at the beam center ($ij = 00$), so that $\max_{ij}(V_{ijk}) = V_{00k}$. Notice that all pixels which can be measured at one arbitrary η_k value will also be accurately measured at all η_k

values, thanks to the tuning of the integration time. Therefore since the dynamic range at a given integration time Δt_k is close to 3 decades (in the absence of parasitic light), the pixels whose polarization can be fully analyzed in detail are those with grey levels lying between $\max(V_{ijk})$ and $\max(V_{ijk})/1000$. Though this remark may appear insignificant for the direct beam, it may play a key role for scattering patterns whose pixel curves are not necessary proportional (mainly bulk patterns), hence preventing the optimization of the integration time.

Intensity measurements of the direct beam are given in Fig. 2 with the rotator tuned at $\phi = \pi/4$. The left figure is for the minimum signal (obtained with $\eta = \pi$) and the right figure for the maximum signal (obtained with $\eta = 0$), which allows to check both the dynamic of measurements and the extinction efficiency (4 decades) of the system.

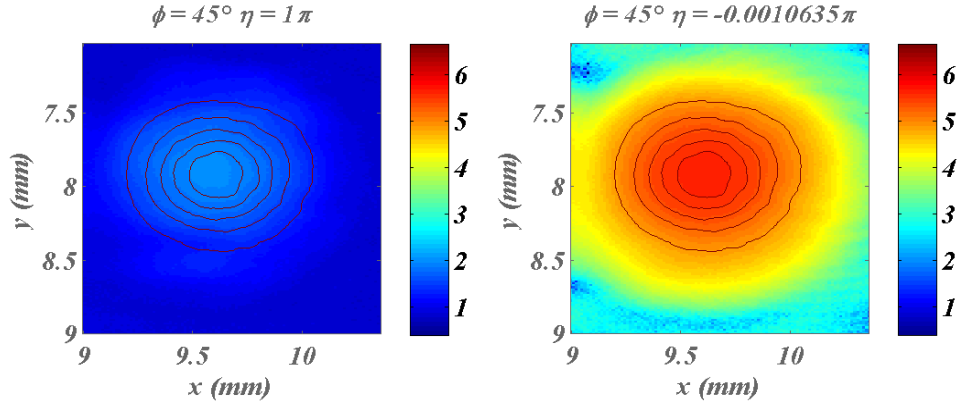


Fig. 2. Minimum ($\eta \approx \pi$ - top figure) and maximum ($\eta \approx 0$ – bottom figure) intensity of the direct beam at the system output, with grey levels on a logarithmic scale. Data are normalized to the integration times. The area of investigation is 1.5mm x 2mm.

The LMS procedure is then applied to the incident beam, that is, to the experimental data of Fig. 2. The number of data points was limited to $N = 20$ phase values (η_k), in order to reduce the acquisition time of the system (less than 5mn). In Fig. 3 are given the cartography of the first parameters δ and α_{45} extracted from measurements at $\phi = 45^\circ$. As expected, these parameters remain around $\delta \approx 0^\circ$ and $\alpha_{45} \approx \text{unity}$, respectively.

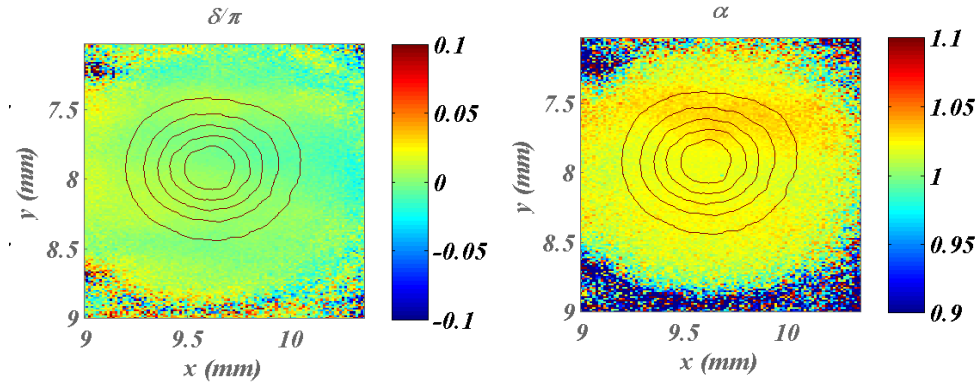


Fig. 3. Cartography of first extracted parameters δ and α .

In a second step the polarization degree is extracted and plotted in Fig. 4 (right figure) with its whole mapping in the area under study. As expected the dop value is quasi-unity (dop

≈ 1) over the whole region of available data, that is, over a dynamic range close to 3 decades (see Fig. 2, right).

To go further in the accuracy of data, we also plotted in Fig. 4 (left figure) the cartography of the normalized distance D_{ij} between the intensity data curves V_{ijk} and those provided by the LMS analytical function, that is, for each pixel:

$$D_{ij} = \frac{\sigma}{m} = \frac{1}{\langle M_{ij,k} \rangle_k} \sqrt{\frac{1}{N} \sum_k \{M_{ij,k} - [1 + \alpha_{ij} \cos(\delta_{ij} + \eta_k)]\}^2} \quad (25)$$

This function allows to check the shape of the polarization curve and provides an evaluation of the data accuracy. In Fig. 4 (left) it is lower than 10% within the whole region of unity dop.

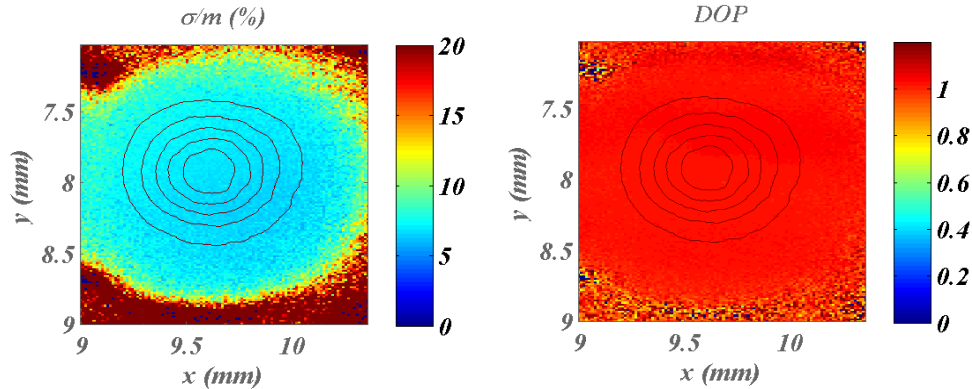


Fig. 4. Mapping of the polarization degree (right figure) and associated normalized distance (left figure).

More information can again be obtained if we emphasize the complete polarization curves for a few pixels chosen with different maximum grey levels (nearly 3 decades). The results are given in Fig. 5 where the polarization curves are plotted in logarithmic scales. We notice the quality of the LMS fit together with the dynamic range of the data whatever the maximum pixel level.

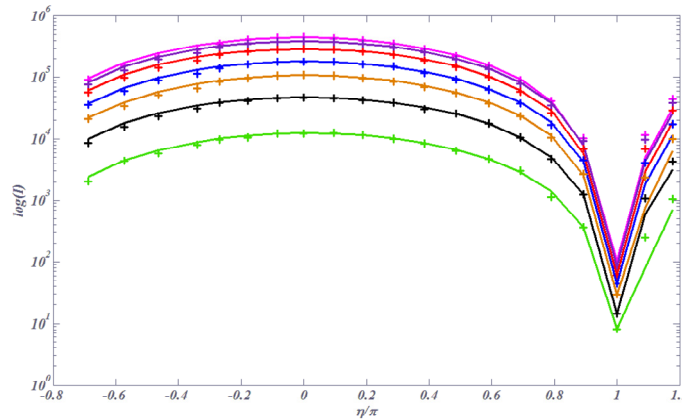


Fig. 5. Polarization curves of a few pixels chosen with different maximum grey levels. *Logarithmic coordinates.*

The last step is to plot the polarization states on the Poincaré sphere for each pixel, what is shown in Fig. 6. A square region of investigation is given on the left figure, and includes a signal variation greater than 2 decades. Such region gathers around 10^4 pixels and the corresponding “data cloud” is emphasized on the sphere (right figure- with a zoom on the top). As expected, the cloud is centered around the incident polarization state (45° linear) and the slight departures from this polarization can be seen as a characteristic of the system performance. Notice that the departures increase with decreasing grey levels; for this reason it is careful to associate a color to each data on the sphere, in order to indicate the maximum grey level (measured at $\eta = 0^\circ$) of the pixel where the polarization state has been measured. Such procedure will be useful to analyze scattering data.

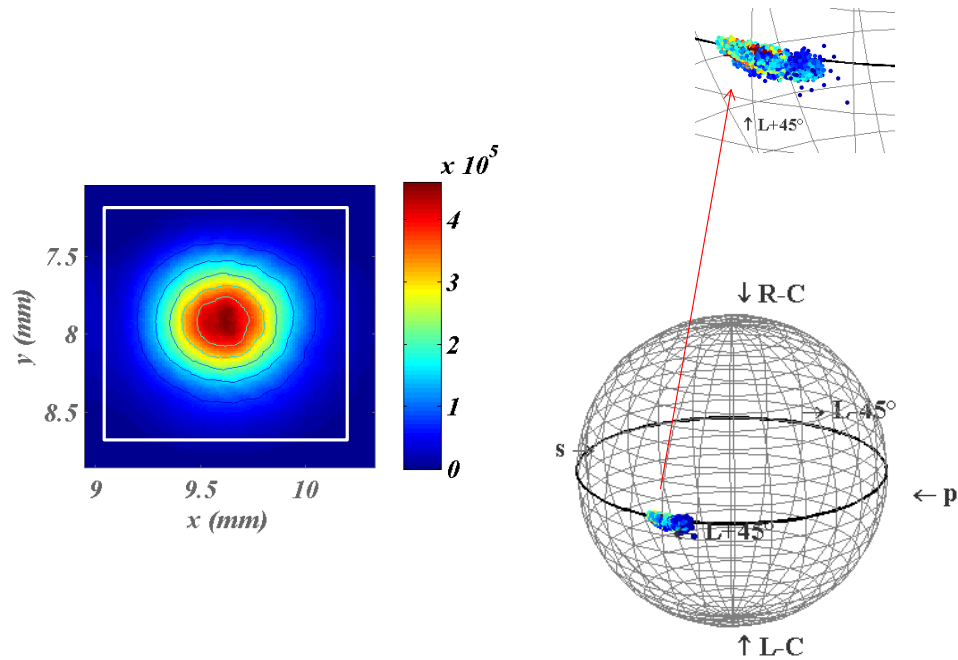


Fig. 6. Polarization states on the Poincaré sphere (right figure- with a zoom on the top), plotted for the square region of the left figure.

Now the probability density functions (pdf) of the dop are given in Fig. 7(a) to summarize most results. The average dop (top figure) is $\langle \text{dop}_{ij} \rangle_{ij} \approx 0.98$ with a root mean square of $8 \cdot 10^{-3}$, which emphasizes the performances limits of the whole procedure. Such performance is in agreement with the fact that the distance function is of the order of 10% within the measurement area. Notice that this dop pdf can also be weighted by the grey levels in order to minimize uncertainty in the measurements, which is also shown in Fig. 7; the difference between the two dop can be summarized as follows:

- The non-weighted (classical) dop emphasizes a dop value taken by N pixels, whatever the grey level (g) on these pixels.
- The weighted dop takes into account the variation of the grey levels g_j within the previous N data points. With $N = \sum_j N_j(E_j)$, the weight of N_j is modified as $N'_j = N_j \cdot g_j / \max(g_j)$

We notice in Fig. 7(a) that a slight percentage of dop values are greater than unity. This is due to the uncertainty of the measurements which provide data from each side of unity, with an average dop lower than unity. To check this point we simulate a beam pattern [16] with

full polarization, but with a random Gaussian noise on each pixel data with 10% root mean square. The result is the histogram of Fig. 7(b) which is similar to that of Fig. 7(a).

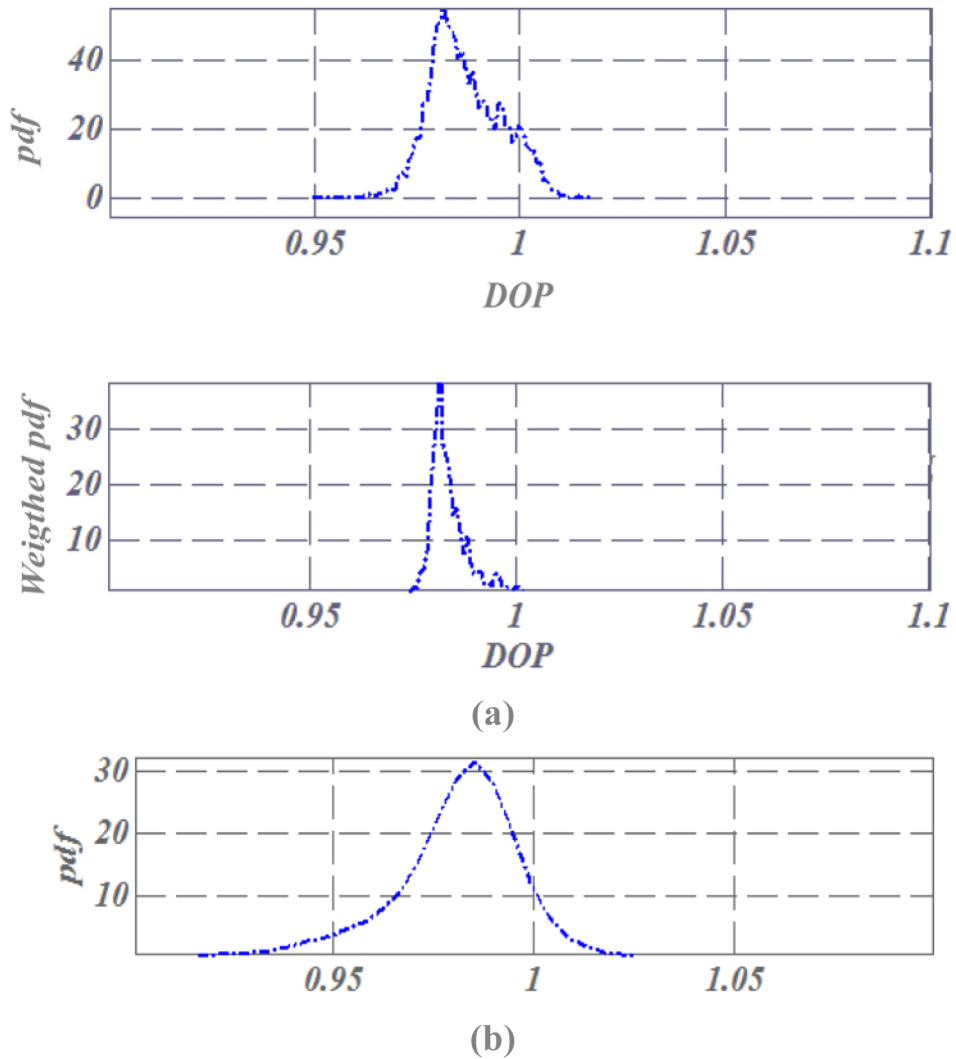


Fig. 7. a: dop histograms measured within the investigation area, weighted (middle figure) or not (top figure) by grey levels (see text). b: calculation of a dop histogram ((see text)) of full polarized pattern in the presence of Gaussian noise with 10% root mean square.

To conclude this section we give in Fig. 8 the histogram of the distance function within the whole CCD area (14mmx14mm), versus the energy levels. Such distance is a criteria for the quality of the LMS fit. Figure 8 clearly gives an overview of the region of validity of most data, that is, the energy levels (nearly 3 decades) where the dop can be measured with an accuracy better than 10%.

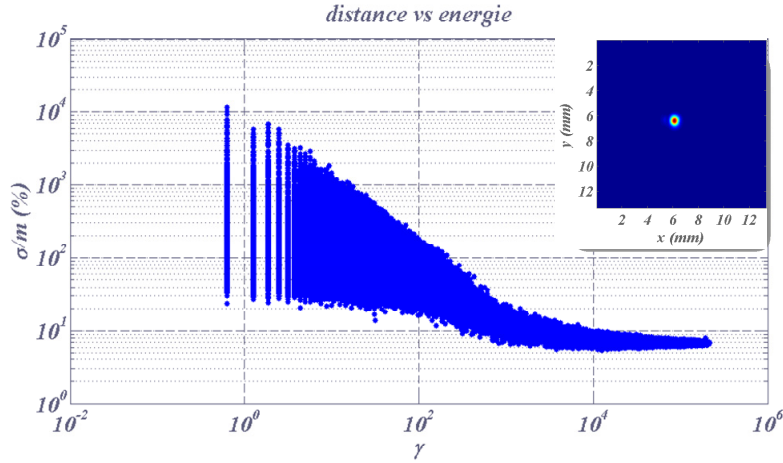


Fig. 8. Histogram of the distance function versus the grey levels. The region of investigation is given at the right, top. The distance provides a criteria for the quality of the LMS procedure (see text).

At this step all results provide a reference and now allow to investigate the polarization of the scattering patterns at the speckle size, what is performed in the next section.

5. Application to surface scattering

The polarization speckle pattern of a rough surface is now investigated at an average direction (15°) in the far field. The illumination incidence is normal with the same laser source, and the set-up is given in Fig. 9. The sample is a high scattering Au surface used for calibration of angle-resolved scattering measurements, that is, a non-absorbing spectral lambertian etalon for the visible spectrum. Notice that the speckle is resolved since the average grain size is $400\mu\text{m}$, while the CCD pixels are $13\mu\text{m}$ in size.

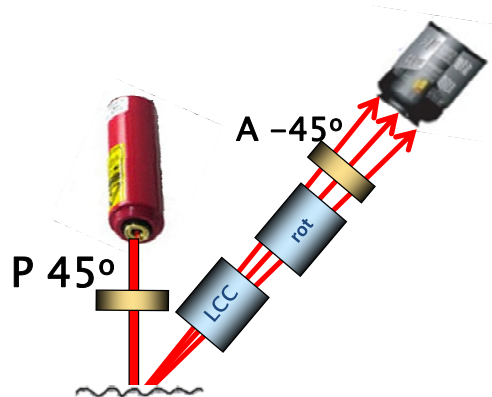


Fig. 9. Basic polarization set-up for analysis of the scattering pattern.

As for the direct beam, this scattering pattern is first plotted in Fig. 10 at the rotator angle $\phi = 45^\circ$, for two specific values of the phase retardation ($\eta = 0^\circ$ and $\eta = 90^\circ$). The situation is different from that of the preceding section since speckle grains have now to be considered, which makes the energy levels to vary in an arbitrary way within the region under study. However in a way similar to the direct beam, the two specific η (0° and 180°) values again provide minimum (left figure) and maximum (right figures) values of the average speckle patterns. This is in agreement with the theoretical results given in [13] which predicted that the polarization ratio β and the correlation argument δ had limited departures from those of

the incident beam ($\beta \approx 1$, $\delta \approx 0^\circ$), depending on the quadratic slope surface. Here the slope average measured with a Zygo microscope was found to be lower than 20° , which explains the results. Therefore all pixel polarization curves are again quasi-proportional and will vanish simultaneously when the phase retardation is scanned, which allows optimization of the integration time. Hence this integration time Δt_k is again chosen for the maximum speckle value measured at $\eta = 0^\circ$ over the ij pixels, that is, for $\max_{ij} (V_{ij0})$. We notice in Fig. 10 that the extinction efficiency of the system approaches 4 decades, a result similar to that of the direct beam.

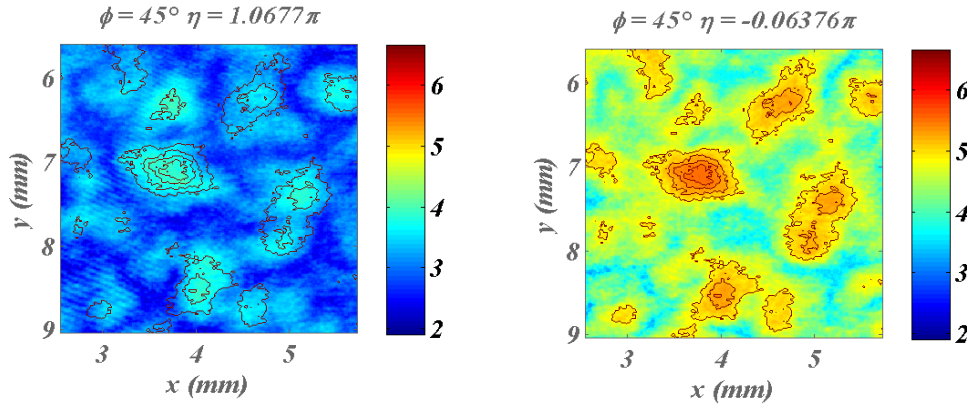


Fig. 10. Minimum ($\eta = \pi$ - left figure) and maximum ($\eta = 0$ - right figure) intensity of the scattering pattern at the system output, with the grey levels in logarithmic scale. Data are normalized to the integration time. The area of investigation is $3\text{mm} \times 3.5\text{mm}$.

The parameters α and δ extracted at $\phi = 45^\circ$ are then plotted in Fig. 11 with their whole mapping. As expected their values roughly remain close to $\delta \approx 0^\circ$ and $\alpha \approx 1$ respectively, though the root mean square is now larger (see the histograms further).

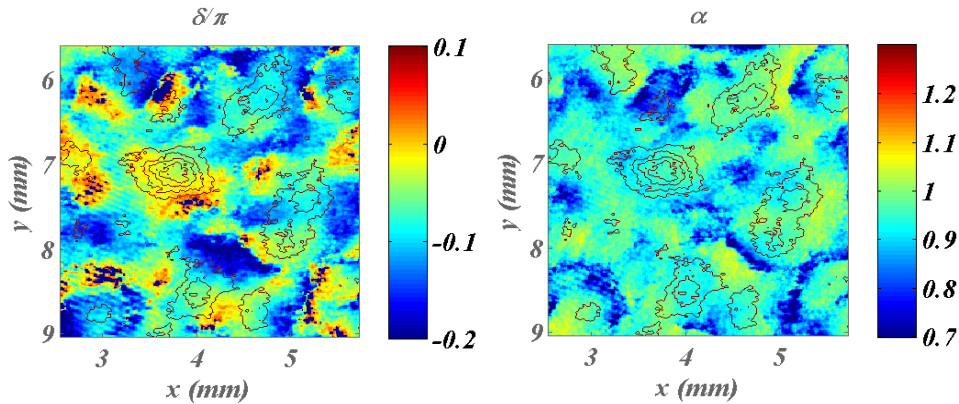


Fig. 11. mapping of the parameters α and δ for the surface scattering pattern.

Key results are plotted in Fig. 12, where the dop cartography and its associated normalized distance are pointed out. The average dop is high as predicted in [13]. Furthermore the distance function is of the same order (lower than 12%) than that of the specular beam, which confirms a similar quality for the scattering pattern analysis.

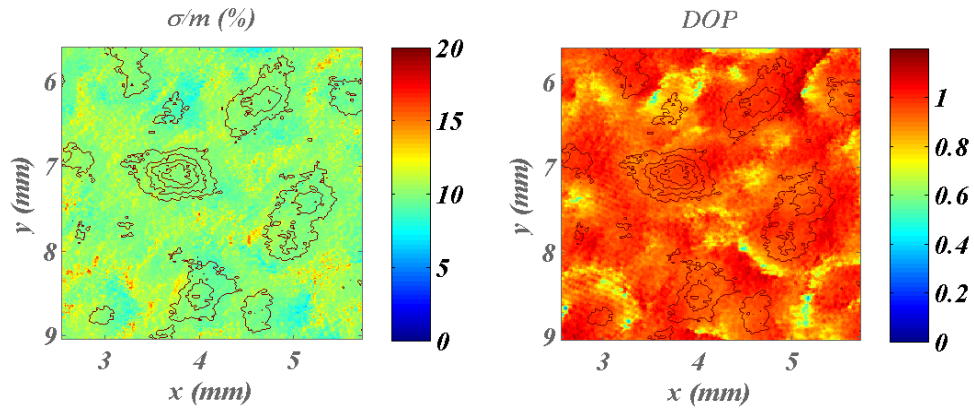


Fig. 12. mapping the dop (right figure) of the surface scattering pattern and its associated distance (left figure).

It is interesting to address the question of the dop variations (even though some %) at the frontiers of the speckle grains. Such slight variations of the dop are not predicted by electromagnetic theory and are suspected to be the result of the measurements accuracy at the low levels of the frontiers. To address this point we plotted the complete polarization curves for different pixels along a line crossing the frontiers, as shown in Fig. 13. We observe that the dynamic remains high when crossing the speckle grain and the slight variations can be attributed to the performances of the whole procedure.

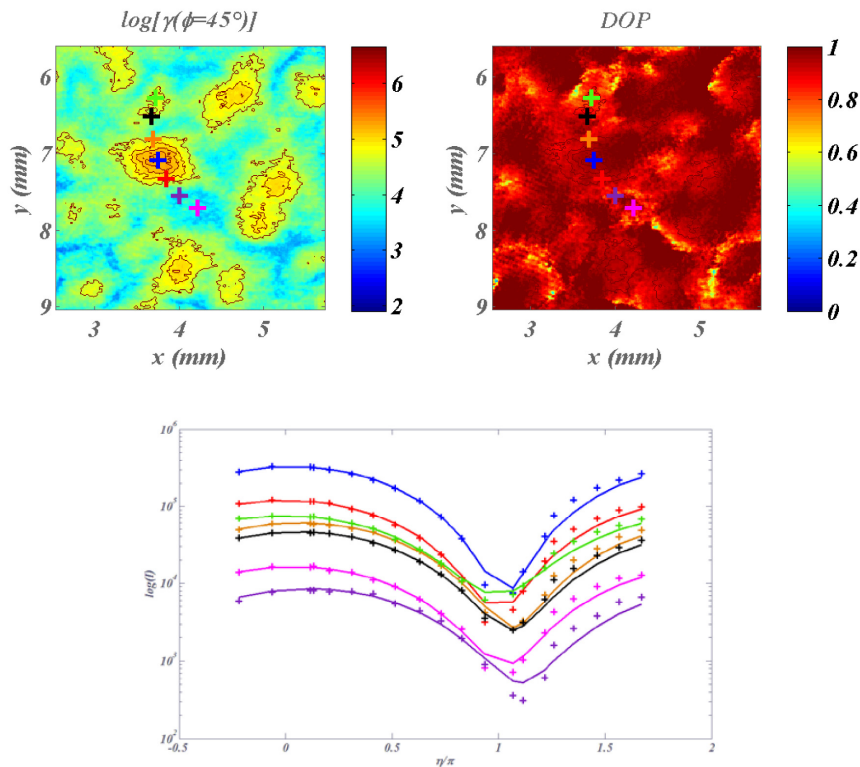


Fig. 13. complete polarization curves (bottom figures) measured for the pixels identified in the top figure across the frontiers of a grain size.

Let us now consider the polarization states on the Poincaré sphere (Fig. 14). For that we chose again 3 different regions within the speckle pattern and for each of them we plotted the resulting “data clouds” on the sphere. In comparison with the results of section 1, we observe a larger departure from the incident polarization state. Notice however that a limited region of the sphere is concerned by the departures so that the global polarization state remains around the incident one. This explains why all speckle grains vanish at the same time when the retardation phase is scanned, and this is in agreement with the theoretical predictions given of [13]. In other words, the surface scattering pattern remains quasi-fully polarized so that the polarization state keeps the memory of the incident one. Notice also that the colors on the sphere allow to specify the grey level of the pixel whose polarization state is plotted.

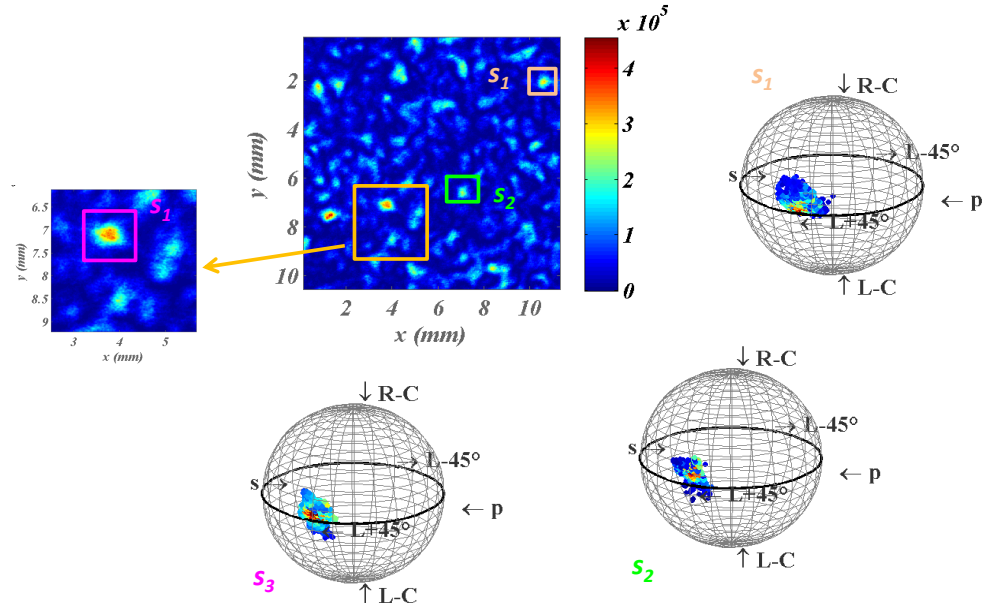


Fig. 14. Polarization states on the Poincaré sphere for different areas within the speckle pattern.

The last point to discuss is the dop histogram of the scattering pattern given in Fig. 15 (top). The average dop is $\langle \text{dop}_{ij} \rangle_{ij} = 0.94$ with a root mean square of $9.4 \cdot 10^{-2}$, larger than that of the direct beam ($8 \cdot 10^{-3}$). These values are close to those of the incident beam, so that no significant temporal (local) depolarization has occurred, as predicted for most surfaces in [13]. One can also use a dop value weighted by the energy levels, which increases the accuracy of measurements (Fig. 15, bottom).

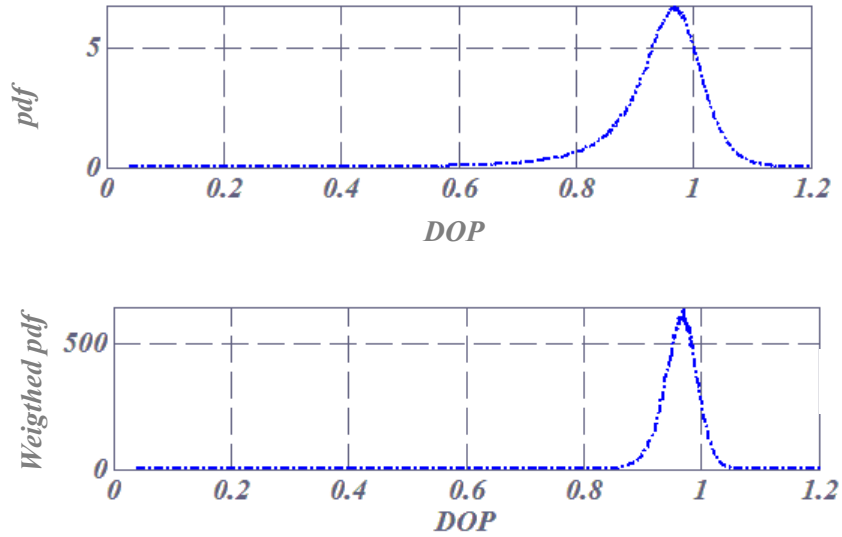


Fig. 15. dop histograms of the scattering pattern, *weighted (bottom) or not (top) by the energy levels.*

To conclude this section we also give the distance function versus the grey levels in Fig. 16. It is lower than 20% over 2 decades.

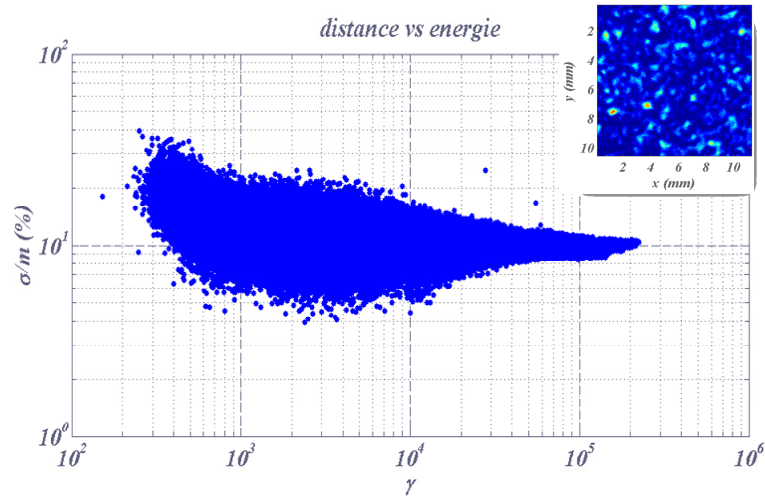


Fig. 16. Distance function of the scattering pattern versus the grey levels. The region of investigation is given at the right, top. The distance provides a criteria for the quality of the LMS procedure (see text related to Fig. 8).

6. Conclusion

A whole procedure and set-up was developed to measure with great accuracy the polarization degree within each grain of the speckle pattern emitted by a disordered medium. Ellipsometric principles were involved and required LCD and rotator devices, together with a high sensitivity camera and LMS procedures. The system performances were first quantified with the direct (specular) beam in order to emphasize a reference or calibration point, to be compared with further scattering data. This reference point is crucial.

In a second step data from a high scattering Au surface were analyzed in detail. Whole mappings were measured for the polarimetric phase and polarization ratio, as well as for the polarization degree. A distance function was associated to all mappings, in order to quantify the accuracy of the results. Such function was also given versus the grey levels. Full polarization curves were pointed out on a line crossing the speckle grains.

In a last step the polarization states were plotted on the Poincaré sphere and confirmed the “scattering clouds” predicted in [13]. As expected, moderate departure is observed on the sphere, which makes the scattering pattern to keep the memory of the incident polarization. Such results are specific of surface scattering and are in high agreement with electromagnetic calculation [13]. Further predictions remain to be confirmed with this set-up and concern bulk scattering [11] and enpolarization effects [16].

Acknowledgments

This work was supported by the French National Research Agency (ANR).